Egypt. J. Chem. **Vol. 68,** No. 10 pp. 609 - 620 (2025)

Egyptian Journal of Chemistry

http://ejchem.journals.ekb.eg/

Controllable of Fabrication Mesoporous Cu/TiO_2 Decorated with g-C_3N_4 Nano-sheets for Improved MB Dye Removal

Sayed M. Saleh,* Hanan A. B. Alharbi, Abueliz Modwi*

Department of Chemistry, College of Science, Qassim University, Buraidah 51452, Saudi Arabia

Abstract

The utilization of a novel heterogeneous photocatalyst for the photodegradation of organic pollutants under visible light is regarded as a significant and indispensable approach for ensuring a sustainable and safe environment, both in laboratory settings and on a larger scale. Therefore, a novel nanocomposite Cu-TiO_2@g-C_3N_4 consisting of mesoporous pure graphite g-C_3N_4 and Cu-TiO_2 was synthesized using a sol-gel technique combined with ultrasonic treatment. The crystal structure of Cu-TiO_2 was conclusively verified using the X-ray diffraction pattern and incorporated into the g-C_3N_4 structure. The Cu-TiO_2 nanoparticles were observed to have a spherical shape based on the SEM images and were evenly distributed throughout the g-C_3N_4 nanosheets. The efficacy of Cu-TiO_2@g-C_3N_4 nanocomposites as a novel photocatalyst for degrading MB dye under visible light was investigated. Cu-TiO_2@g-C_3N_4 had a synergistic effect on the photocatalytic activity associated with the degradation of MB dye.

Keywords: Cu/TiO_2@g-C_3N_4; nanocomposite; ultrasonic; MB dye, Water contaminations

1. Introduction

A major issue that has arisen in recent decades as a result of industrialization, urbanization, and the economic revolution is water pollution. Organic pollutants, such as pesticides, dyes, and pharmaceuticals, among others, are liberated into water reservoirs and have a serious negative impact on the ecosystem because they don't degrade easily. As a result, experts are becoming more interested in water filtration to lessen the negative impacts of pollution. Dyes generated from textile, paper, and paint industries are only a few of the organic pollutants that are dumped into the water [1-3]. Due to the presence of heavy metals, aromatic chemicals, and dye molecules in industries, they play a significant role in deteriorating the ecosystems [4,5]. Dye exposure in aquatic habitats puts living things at risk for illness, reduces light penetration into the water, which lowers the effectiveness of aquatic plants' photosynthetic processes, and also creates anoxic conditions that have an influence on aquatic fauna and flora [6]. Due to the enduring colors, they diminish the aesthetic value of aquatic bodies and raise the need for biological and chemical oxygen [7]. Additionally, they accumulate in the food chain and induce toxicity, which causes a variety of serious health issues [8].

Methylene blue (MB) is an aromatic heterocyclic basic dye, a renowned cationic and primary thiazine dye having a $C_{16}H_{18}N_3ClS$ molecular formula, and $\lambda_{max} \approx 660$ nm [9]. The MB finds various useful biomedical applications as an active therapeutic means to treat anemia, and malaria, along with its use in human and veterinary drug for numerous diagnostic and therapeutic processes. In the industrial sector, MB dye has lots of applications in the fabric, pharmaceuticals, pulp and paper, coloring, paints, and food [10]. The release of MB above a certain concentration from the industrial facilities in natural water sources poses a serious health menace to human beings and other living organisms. The MB is noxious, carcinogenic, and non-biodegradable and can induce a serious hazard to human wellbeing and have a damaging impact on the environs [11]. It can cause several threats to human health, including respiratory distress, visceral disorders, loss of sight, and gastrointestinal and mental ailments [12-14]. The purification of MB dye contaminated water prior to discharging into the environment is of vital significance due to its risky effects on water quality and health [15]. A number of approaches have been adopted to eliminate MB and other dyes from industrial wastewater.

These methods include coagulation, phytoremediation, adsorption/biosorption, biodegradation, nanofiltration, electrocoagulation besides others. Every one of these management techniques has its merits and limitations concerning cost-effectiveness and viability, competence, and environmental sway [16-19]. As heat and light stable and non-biodegradability, it is usually hard to break down MB dye into smaller inorganic compounds using classical protocols [20]. MB is broken down into innocuous chemicals such CO_2, H_2O, NH_4^+, SO_4^{2-}, and NO_3^-, making photo-catalysis superior to other approaches [21, 22].

As an effective photo-catalyst with a lot of surface area in this context, TiO_2 semiconductor material is frequently used to address environmental problems by destroying organic pollutants from industrial wastewaters and reducing the amount of heavy metals [23-25]. TiO_2, with a 3.2 eV band gap, is often exclusively active in the UV spectrum, which limits its applications in

*Corresponding author e-mail: e.saleh@qu.edu.sa (Sayed M Saleh)

Receive Date: 26 March 2025, Revise Date: 13 May 2025, Accept Date: 18 May 2025

DOI: 10.21608/ejchem.2025.371486.11523

the visible spectrum [26]. For increased sensitivity to visible light, TiO_2 has been doped with non-metals like N, C, and S as well as metals as Fe, Cu, and Mn [27-29]. Despite the fact that generally lowering the band gap increases photocatalytic activity in visible light, the photocatalytic activity in visible light is diminished as a result of electron hole pair recombination. Because of this, TiO_2 has been coupled with other semiconductors to generate kind I and kind II heterojunctions, which improve the charge separation. Semiconductors like WO_3, Fe_2O_3, BiO, and MoS_2 form kind I heterojunctions when combined with TiO_2 [30, 31] whereas kind II heterojunctions are formed by semiconductors like CuO, CdSe, V_2O_5, CeO_2, Bi_2S_3, WS_2, and Bi_2O_3 [32-34]. A cheap precursor for example urea, cyanamide, melamine, etc. is typically used to create the metal-free semiconductor g-C_3N_4.

The sheets have a honeycomb-like structure and are made up of s-triazine or tri-s-triazine units like the structural monomers. Vander Waals forces hold the sheets together whereas covalent bonds bind the atoms in one sheet [35-37]. In order to maximize the charge separation, g-C_3N_4 has also been coupled with other substances such as TiO_2, ZnO, Fe_2O_3, SnO_2, V_2O_5, Bi_2O_4, α-MoC1-x quantum dots, charcoal, etc. An issue that results in reduced photocatalytic activity when g-C_3N_4 is taken individually is electron-hole pair recombination [38-40]. To prevail over the large band gap energy of the TiO_2 and the high electron-hole pair recombination rate of the g-C_3N_4 Cu doped TiO_2 and g-C_3N_4 were combined to form a z-scheme heterojunction in order to test the photocatalytic activity of the new nanocomposite in the photodegradation of MB. Additionally, the manufacturing of the novel g-C_3N_4-Cu-TiO_2 composites was ecofriendly, necessitating no use of rigid templates or harmful solvents.

2. Experimental

2.1. Synthesis of g-C_3N_4 nanosheets

A set method was assumed to create the pure g-C_3N_4 nanomaterial. Carbonyl diamide (4.5 g) was butted in a crucible with aluminum foil cover and then annealed in a muffle furnace at 500 °C for 2 h with a heating rate of 10 °C/min at the room temperature. Following consistent cooling, the yellow powders were received.

2.2. Construction of Cu-TiO_2 NPs

C_2H_5OH, CH_3COOH and HCI were mixed in a container in the sequence of 60, 10 and 1 mL followed by dispersing F-127 (3 g) in this mixture. After that, the attained mixture was utilized to disperse titanium dioxide and copper (II) nitrate in the sequence of 4 g and 1 g utilizing strong agitation. The attained sol was separated from the previous solution and then C_2H_5OH was removed via heating for 24 h at 50 °C followed by extra heating overnight at 85 °C for dehydration. Finally, F-127 surfactant was eliminated from the gel via heating at 400 °C for 2 h to provide the required Cu-TiO_2 NPs.

2.3. Fabrication of Cu-TiO_2@g-C_3N_4 photocatalyst

0.6 and 3.4 wt.% Cu-TiO_2@g-C_3N_4 photocatalysts were constructed via achieving high distribution of the prepared Cu-TiO_2 NPs over the produced porous g-C_3N_4 nanosheets and then stirred in a 100 mL of methanol for 15 min. The previous mixture was sonicated for 60 min to assure the good dispersion of the solid specimen throughout the solution and then oven-dried at 70 °C for 24 h (Scheme 1).

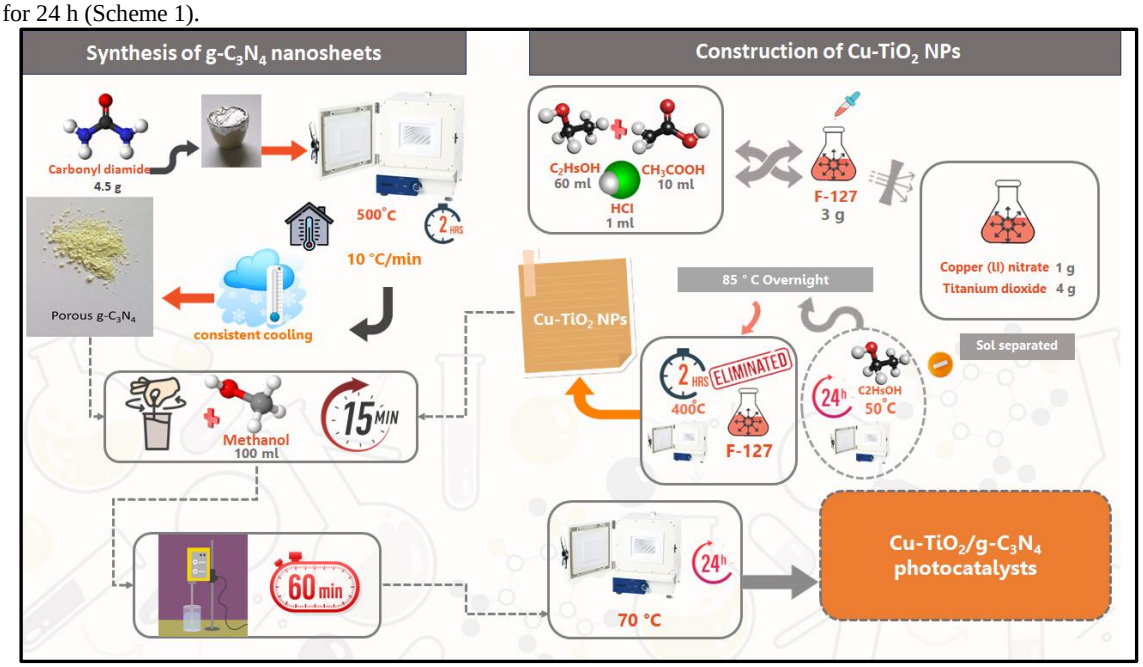

Scheme 1. The Cu-TiO_2@g-C_3N_4 photocatalysts steps.

2.4. Characterization

Using monochromate Cu Ka radiation, X-ray diffraction (XRD) patterns were captured in a PANalytical diffractometer (Model PW3040/60) X'pert PRO. A ZEISS Sigma 500 was used to measure the patterns of the samples used for scanning electron microscopy (SEM) and energy dispersive X-ray spectroscopy (EDX). On a JEM-2100 apparatus, examinations using transmission electron microscopy (TEM) and high-resolution transmission electron microscopy (HRTEM) were performed. On a Thermo Nicolet IR200, Fourier transform infrared (FT-IR) spectra data were collected. On a Quantachrome Instruments 2SI-MP-20, the surface areas of samples measured by Brunauer- Emmett-Teller (BET) were calculated. Using an Al Ka radiation

excitation source, X-ray photoelectron spectroscopy (XPS) experiments were carried out using a Thermo Scientific Escalab 250Xi spectrometer. On a PerkinElmer Lambda 950, the UV-vis diffuse reflection spectra (DRS) were collected. At an excitation wavelength of 350 nm, PL spectra were discovered using a Cary Eclipse fluorescence spectrometer.

2.5. Photocatalysis procedure

Several degradation tests were carried out to determine the optimal conditions for the MB dye degradation process based on Cu-TiO_2@g-C_3N_4 nanomaterials. The effects of important factors on the degradation process were evaluated. These characteristics included the starting concentration of MB, the concentrations of the nano-catalysts, and the pH measurements of the mediums that were analyzed. All the tests were carried out based on optimal circumstances, with a volumetric flask containing 2 milliliters of MB solution at a 25 parts per million concentration. A pH adjustment was performed on each test that was measured using 0.1 MHCl and 0.1 MNaOH. Magnetic stirring was done for ten minutes at a speed of 4400 revolutions per minute on the mediums of the MB dye and the Cu-TiO_2@g-C_3N_4 nano-catalysts colloidal mixes that were being evaluated. To get the UV/Vis spectra of the MB solutions, the Evolution^{TM} 200 series Thermo Fisher Spectrophotometer (located in Waltham, Massachusetts, United States) performed the analysis.

3. Results and Discussions

3.1. Nanostructures characterization

The XRD graphs (Figure 1) were used to determine the phase structures of the synthesized nanostructure. The pristine g-C_3N_4 reveals the characteristic nitride peaks at 13 and 27.33°. The High-intensity peak at around 27.33◦ is a distinctive feature

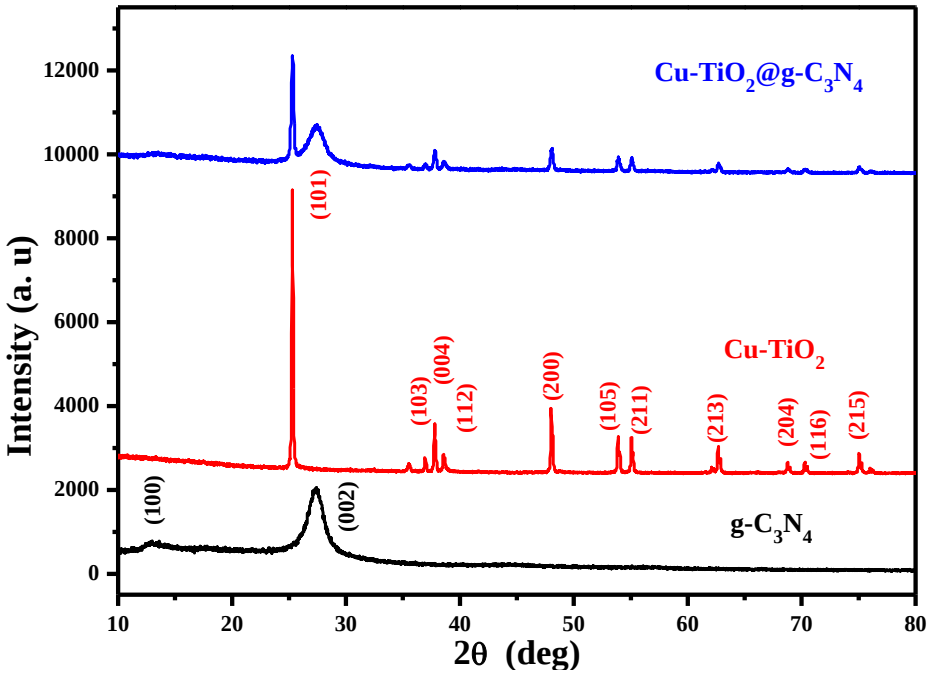

Figure 1. The XRD of the g-C_3N_4, Cu-TiO_2, and the Cu–TiO_2@g-C_3N_4.

for the (002) interlayer stacking reflection of conjugated aromatic fragments. The computed interlayer distance of aromatic units (d = 0.3261 nm), which is identical to that of the crystalline g-C_3N_4 [41]. The minor peak can be indexed as (1 0 0), is germane to the in-plane organizational repeating design, like the hole-to-hole distance of the uninterrupted tri-s-triazine pores. The mutual occurrence of these well-resolved diffraction peaks ascertains the development of C_3N_4 framework [42]. The XRD Cu-TiO_2 nanoparticles displayed diffraction peaks at 2θ of 25.3°, 37.0°, 37.8°, 38.7°, 48.0°, 53.9°, 55.0°, 62.8°, 68.8°, 70.3°, and 75.0° which sequentially resemble to the (101), (103), (004), (112), (200), (105), (213), (204), (116), and (215 crystal planes of the anatase TiO_2 phase (JCPDS No. 21-1272) [43].

There was neither rutile TiO_2 phase nor $CuTiO_3$ observed in the spectrum as the synthesis was done at relatively low temperature. In addition, no diffraction peaks of Cu or Cu oxides in Cu-TiO_2 were perceived, which may be reasoned by for the high dispersion of any related phase within TiO_2 crystal lattice or that the amount of Cu or Cu oxides is lower than the XRD detection limit [44-46]. Furthermore, the ionic radius of Cu^{2+} (73 pm) is fairly comparable to the ionic radius of Ti^{4+} (74 pm) and thus the Cu^{2+} could interstitially or substitutionally replace Ti^{4+} in the Anatase phase of TiO_2 lattice [47]. The XRD patterns of the ternary Cu-TiO_2@g-C_3N_4 include both the Cu–TiO_2@g-C_3N_4 peaks. However, the merging of the two entities resulted in the reduction of peak intensities along with the change in broadening of the (002) nitrides peak from β = 1.2623 to β = 1.3173 and that of the (101) of the Cu–TiO_2 from β = 0.1321 to β = 0.2058. The crystallite size (*D*), lattice strain (ε), and the lattice parameters (*a*, *b*, *c*) were calculated using the following expressions:

$$D = \frac{0.9\lambda}{\beta\cos\theta} \qquad (3)$$

$$\frac{1}{d^2} = \frac{h^2+k^2}{a^2} + \frac{l^2}{c^2} \quad (4)$$

$$\varepsilon = \frac{\beta_{hkl}}{4\tan\theta} \quad (5)$$

Due to the incorporation of nitride into the Cu-TiO_2 considerable alterations in the structural characteristics as the crystallite size of the g-C_3N_4 decreased from 6.48 to 6.21 nm, while the change in the Cu-TiO_2 was from 61.67 to 39.58 nm. These reductions in sizes were accompanied with an increase in the lattice strain the augmented from 0.0226 to 0.236 for the nitride and 0.0026 to 0.0040 for the Cu-TiO_2. The lattice parameters for the Cu–TiO_2 were found to be a = b = 3.7896 and c = 9.4521 nm before and a = b = 3.7857 and c = 9.5123 nm after the ternary composite. This result infers that the amalgamation of the g-C_3N_4 had changed the Cu–TiO_2 nanoparticles growth along the *c-axis*. Such behavior was attributed to an anisotropic growth [48].

Fourier-transform infrared (FT-IR) spectroscopy is a strong analytical technique for determining and characterizing the chemical composition of materials (Figure 2a). When applied to the study of pure Cu-TiO_2, pure C_3N_4, and Cu-TiO_2@g-C_3N_4, FT-IR analysis can reveal important information on the molecular structure, functional groups, and chemical interactions present in these materials. Pure Cu-TiO_2 is a composite material made from copper (Cu) and titanium dioxide (TiO_2). The FT-IR spectra of pure Cu-TiO_2 may have characteristic peaks corresponding to the vibrational modes of Cu-O and Ti-O bonds at ≈ 500 cm^{-1} [49]. The presence of these peaks would indicate the presence of Cu and TiO_2 in the samples. Pure C_3N_4 is a carbon nitride substance noted for its great stability and catalytic activity. The FT-IR spectrum of pure C_3N_4 should show peaks corresponding to C-N and N-H bonds, which are characteristic of the C_3N_4 structure. Cu-TiO_2@g-C_3N_4 is a composite material that combines Cu-TiO_2 nanoparticles with graphitic carbon nitride. The FT-IR spectra of this composite should show peaks corresponding to the vibrational modes of Cu-O, Ti-O, C-N, and N-H bonds, showing the presence of all components in the composite material. The intense peaks at 1250, 1300, 1412, and 1598 cm^{-1} were attributed to aromatic C-N stretching vibration modes, and a peak at 1650 cm^{-1} was assigned to C-N heterocycle stretching vibrations, while the prominent band about 3240 cm1 was for -OH stretching vibrations [50]. Furthermore, in the FTIR spectra of TiO_2 NPs, -OH group stretching was observed at 3400 cm^{-1}, with peaks at 1630 and 480 cm^{-1} are attributed to the bending modes of water Ti-OH and the stretching frequency of Ti-O-Ti [51].

Photoluminescence (PL) spectroscopy analyses were implemented in order to disclose the recombination rate of photogenerated charge carriers (electron–hole pairs) [52]. The photogenerated charge carriers separation has a vital role in the photocatalytic competence of the photocatalyst. A great separation rate leads to higher photocatalytic action [53]. The PL graphs of the g-C_3N_4, Cu-TiO_2 and Cu-TiO_2@g-C_3N_4 (Figure 2b) shows and absorption at longer λ for the g-C_3N_4, and Cu-TiO_2@g-C_3N_4 than Cu-TiO_2 which connotes a better visible light activity. Relative to the Cu-TiO2, the PL emission intensity of g-C_3N_4 and Cu-TiO_2@g-C_3N_4 photocatalyst decreased noticeably. The lowest intensity of the Cu-TiO_2@g-C_3N_4 compared to the pure g-C_3N_4 reveals that the fabricated photocatalyst interface can function as competent transfer channels for charge carriers [54]. Henceforth, the migration of photogenerated charge carriers between Cu-TiO_2 and g-C_3N_4 was enhanced, bringing about lower PL intensity and better-quality photocatalytic performance for the ternary Cu-TiO_2@g-C_3N_4 composite.

The UV-Vis DRS of Cu-TiO_2, g-C_3N_4 and Cu-TiO_2@g-C_3N_4 are portrayed in Figure 2c. The Cu-TiO_2 revealed an absorption in the shorter wavelength of the UV region with optical edge at ≈ 380 nm. The pure g-C_3N_4 showed relatively higher photon absorption extending towards the visible light region with an optical edge at ≈ 430 nm as a characteristic feature of the visible light driven activity of the nitride [55]. The absorption of Cu-TiO_2 is extra shifted to the visible range after g-C_3N_4 incorporation signifying high visible light absorption. This finding proves that g-C_3N_4 addition stretched light absorption to a longer wavelength, indicating that g-C_3N_4 acts as sensitizer. The optical band gap was computed using the Tauc formula [56]:

$$\alpha h\nu = A(h\nu - E_g)^n \quad (6)$$

Here the symbols α, A, $h\nu$ and E_g symbolize the absorption coefficient and optical transition-dependent constant, the photon energy, and the material's band gap energy. The value of the power "n" identifies the type of the semiconductor's optical transition. The n value is taken as 0.5 for allowed direct optical transitions [57]. The value of optical band gap energy can be obtained by extrapolating the linear part of the plot intersects the energy axis (αE = 0) corresponds to the value of E_g (Figure 2d). The band gap energies of the Cn Cu-TiO_2, g-C_3N_4 and Cu-TiO_2@g-C_3N_4 were estimated respectively as 3.33, 2.99, and 2.96 eV. Similar band gap lowering due to metal oxides incorporation into nitride due to the more negative potential of the N_{2p} orbital compared to the O_{2p} orbital in metal-oxides. In addition, the sensitization effect of g-C_3N_4 on TiO_2/g-C_3N_4 photocatalyst could be the reason to the lower band gap value of TiO_2/g-C_3N_4 photocatalyst when compared to that of pristine TiO_2. Typically, g-C_3N_4 has been doped to improve its photo-electronic functionality and the reason for that is the layered assembly of g-C_3N_4 encompasses voids that can host heteroatoms, stimulating a conduction band move up to improve light absorption [58].

Figure 3 exhibits the morphology of the g-C_3N_4, Cu-TiO_2 and Cu-TiO_2@g-C_3N_4 and the EDX analysis for the elemental composition of the nanostructures. The SEM of the g-C_3N_4 (Figure 3a) shows flaky sheet-like structures that are stacked and layered and these formed 2D sheets enfold and crumple in some areas. The SEM of the Cu-TiO_2 (Figure 3c) shows agglomerated nanoparticles which may had due occurred due to their high surface energy, secondary crystallization, and/or Ostwald ripening. The Cu-TiO_2@g-C_3N_4 SEM image (Figure 3e) depicts the flaked structures of g-C_3N_4 with dispersed nanoparticles of Cu-TiO_2 within the surface of the nitride nanosheets.

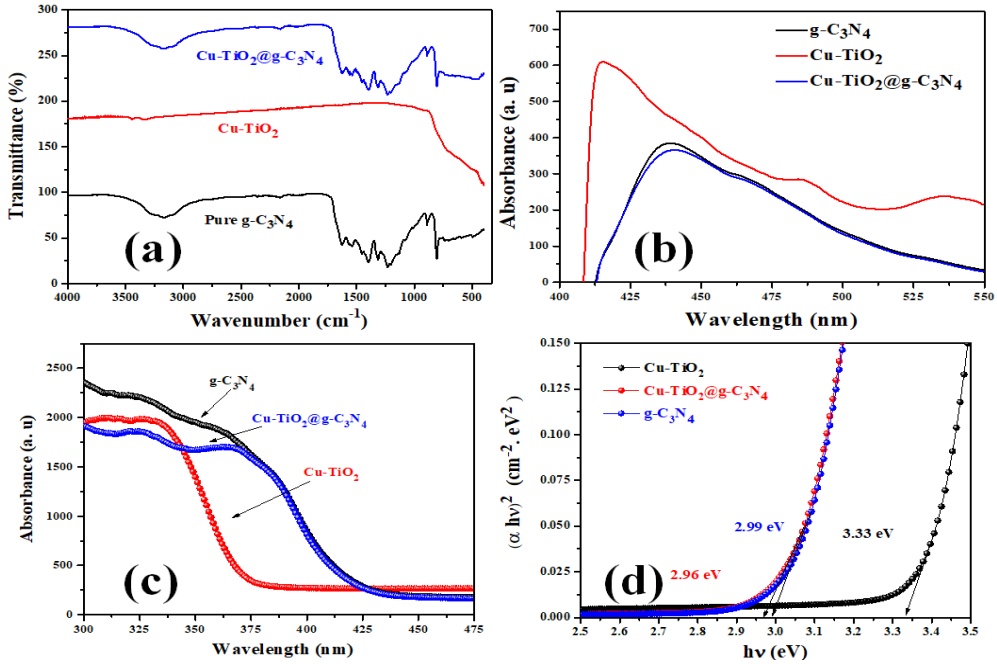

Figure 2. The FTIR (a), PL (b), UV-Vis absorption (c) and Tauc plots (d) of the g-C_3N_4, Cu-TiO_2, and the Cu-TiO_2@g-C_3N_4.

The presence of C and N in the EDX of the g-C_3N_4 (Figure 3b) and the C/N = 0.80 ratio is almost equal to the theoretical value of 0.75 which indicates the successful fabrication of the nitride. The minor oxygen ratio observed in the EDX might be due to the surface oxygen on the sample surface. The elemental composition of the Cu-TiO_2 (Figure 3d) reveals the presence of high Ti and O and low Cu percentages which indicates the very less quantity of Cu. The presence of C might be attributed to some residue of the solvents used for the synthesis of the Cu-TiO_2. The elemental composition of the ternary Cu-TiO_2@g-C_3N_4 composite (Figure 3f) conveys the existence of C, N, Ti, O, and Cu as the primary elements with traces of Cl impurity that may have resulted during the preparation. The successful fabrication of the intended composite can be verified by the obtained EDX results.

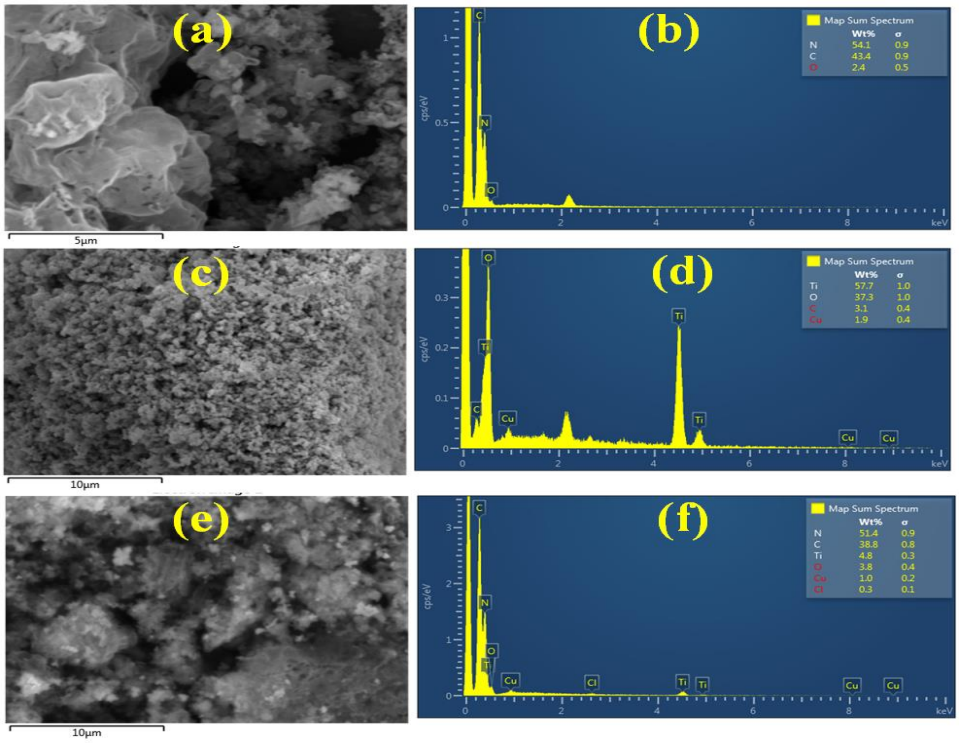

Figure 3. The SEM and EDX of the g-C_3N_4 (a,b), Cu-TiO_2 (c,d), and the Cu-TiO_2@g-C_3N_4 (e,f).

The X-ray photoelectron spectroscopy analyses were performed to confirm the oxidation state of the Cu-TiO_2@g-C_3N_4 composite. The peaks correlating with the $Cu_{2p1/2}$ and $Cu_{2p3/2}$ are apparent at 953.7 and 933.3 eV, respectively (Figure 4a). These values are in consonance with the earlier reported values of CuO [59]. In addition $Cu_{2p1/2}$ satellite peak which is typical for the CuO is evidently witnessed at 942.4 eV, whereas the satellite peak for the $Cu_{2p1/2}$ emerged at 962.6 [60]. Both peaks and their satellites are ≈ 9 eV apart from each other. The XPS peaks positions and the difference between them assent the peaks of copper (II) state with d^9 electron configuration [61].

As illustrated in Figure 4b, the binding energies at 458.0 and 463.7 eV match with the $Ti2p_{3/2}$ and $Ti2p_{1/2}$, respectively [62] with the area ratio of $Ti^{4+}2p_{1/2}$ to $Ti^{4+}2p_{3/2}$ was ≈ ***xxx***. The difference in binding energy as a result of spin orbit coupling, $\Delta E_b = E_b$ (463.7 eV) – E_b (458.0 eV) was 5.7 eV, which is agrees well with the reported values [63] and advocate the existence of the Ti^{4+} oxidation state. The detailed XPS spectrum of O1s (Figure 4c) shows a broad peak that could be deconvoluted to two components, which were assigned to the lattice oxygen (529.3 eV), and the hydroxyl groups and/or adsorbed O_2 (at 531.0 eV) [64]. Additionally, the C1s, (Figure 4d) peak was subdivided into three peaks with binding energies of 284.3, 285.1, and 287.7 eV, which could be assigned to the sp^2 C–C bonds, the C-NH_2 species of the g-C_3N_4, and the carbon in N–C=N respectively [65, 66]. Lastly, four peaks were detected in the high-resolution XPS spectrum of N 1s (Figure 4e). The peak at 398.3 eV is allocated to sp2-hybridized aromatic N bound to C atoms (C = N-C) [67], while the peak at the binding energy of 399.0 eV denotes tertiary nitrogen N-$(C)_3$ [68]. The peaks positioned at 400.6 and 404.2 eV were attributed to C-N-H groups [69].

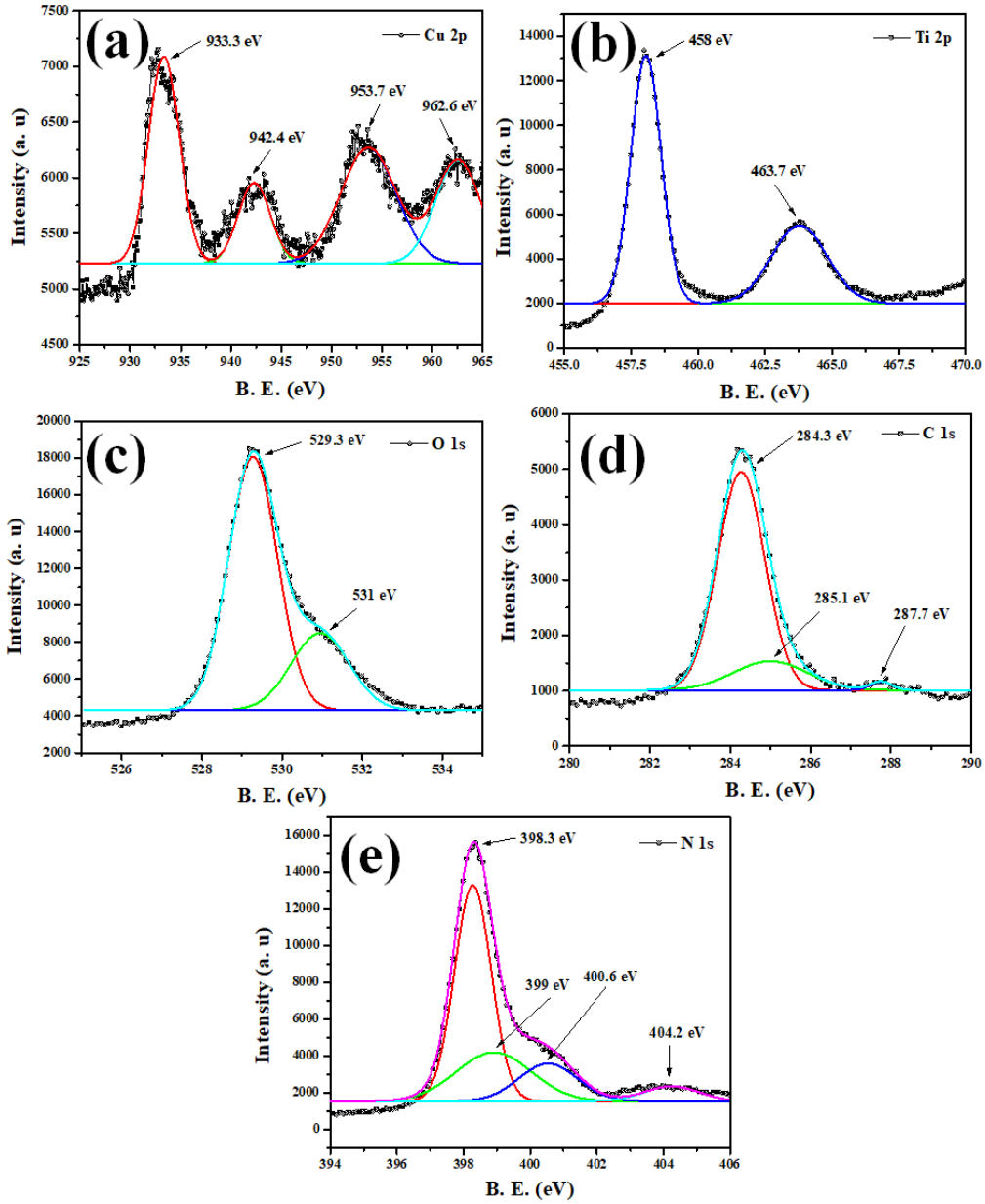

Figure 4. The detailed XPS spectra for Cu 2p (a), Ti 2p (b), O1s (c), C1s (d) and N1s (e).

3.2. MB photodegradation

The photodegradation of MB dye was conducted as a test reaction to assess the photocatalytic performances of the fabricated nanostructures. Figure 5a portrays the degradation efficiency of the Cu-TiO_2, g-C_3N_4 and Cu-TiO_2@g-C_3N_4 under visible light irradiation employing 30 ppm MB, 50 mg of the photocatalyst, at pH 7, and room temperature. The data revealed that the photocatalytic activities were in the following order: photolysis << Cu-TiO_2 < g-C_3N_4 < Cu-TiO_2@g-C_3N_4 within 80 minutes time interval. As a result the MB stability, it is not efficiently degradable by photolysis [9]. The high competence of the ternary Cu-TiO_2@g-C_3N_4 composite was in line with the lowest band gap energy and the lowest recombination rate of the photogenerated electrons-holes pairs.

To measure the heterogeneous photodegradation activity, the Langmuir–Hinshelwood (L-H) model is generally deliberated, as expressed in the following formula [70]:

$$\frac{-dC}{dt} = \frac{kKC}{1+KC} \qquad (8)$$

where the thermodynamic adsorption and photodegradation rate constants are denoted in turn as K and k. As the photocatalyst concentration remains always constant, the reaction kinetics is made simple, and the word "pseudo" is added as a prefix to the reaction rate expression. At high dye concentrations, the photocatalyst surfaces are totally covered, bringing about the estimation of (1 + KC) to KC and pseudo zero-order reaction is, hence, considered for surface saturation coverage. In case of low initial dye concentrations the (KC + 1) ≈ KC and a pseudo first-order rate equation is derived. The equation is useable by presumption that the driving force of degradation is always proportionate to the dye concentration [71].

$$-\frac{dC}{dt} = k_1 C \qquad (9)$$

Here k_1 designate the rate constant for the pseudo-first-order reaction. By integrating the equation under the two boundary conditions becomes

$$ln\left(\frac{C_0}{C_t}\right) = k_1 t \qquad (10)$$

The slope of the linear the plot of *ln* (C_0/C_t) versus the illumination time (Figure 5 b), gives the rate constant of the photodegradation. The half-life or time for the C_t = ½ C_0 is derived from the above equation as $t_{1/2} = ln2/k_1$. Clearly, the $t_{1/2}$ of the first-order model is not dependent on the dye concentration [10]. The kinetics graph for the MB degradation produced straight lines of *ln* (C_0/C_t) vs t plots confirming the pseudo-first order-kinetics of the catalytic degradation process. The Cu-TiO_2@g-C_3N_4 exhibited 1.9 and 3.1- fold rate compared to the g-C_3N_4 and the Cu-TiO_2 respectively as well as the shortest $t_{1/2}$ value (Table 1).

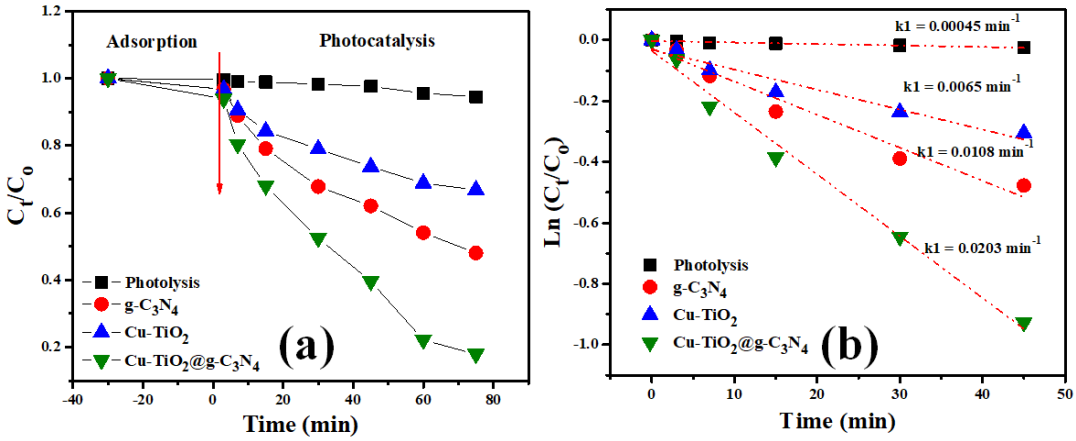

Figure 5. The MB photodegradation efficiency (a) and kinetics (b) graphs.

Table 1: The MB photodegradation kinetics constants

Photocatalyst	Degradation (%)	k_1 (min.)$^{-1}$	$t_{1/2}$ (min.)
Photolysis	5.50	0.00045	1540
Cu-TiO_2	33.2	0.00650	107.0
g-C_3N_4	51.9	0.01080	64.00
Cu-TiO_2@g-C_3N_4	82.9	0.02030	34.00

The pH of photocatalysis setup can be regarded as one of the utmost imperative factors that can seriously impact the dye photo-oxidation process. The pH influence on the MB photocatalytic degradation was probed at the pH range 3-11 (Figure 6a).

The data showed that the solution pH had a direct influence on the heterogeneous photocatalysis. Regarding the positive charge of the cationic MB dye in solution, the influence of pH on its photocatalytic degradation can be justified on the basis of electrostatic adsorption model where cations are easily amassed. At low pH values 3 – 5 the repulsive forces between the positive H^+, and H_3O^+, as well as the protonated amine functional groups on the Cu-TiO_2@g-C_3N_4 surface had greatly diminished the degradation activity. The highest photodegradation was accomplished at pH = 7.0 which agrees with previous [72].

To specify the influential radical species which are involved in the MB photodegradation, the isopropanol (Isop), ascorbic acid (ASC), silver nitrate ($AgNO_3$), and EDTA as the scavengers that respectively suppress the *OH, O_2*, *e* and h^+ [73]. The histograms for the MB degradation percentage (Figure 6b), shows that the ASC significantly reduced the degradation from 90.3 to 4.16 %, followed by Isop that dropped the percentage to 12.19 %, meanwhile the $AgNO_3$ and EDTA decreased the degradation to 36.74 and 53.61% respectively. Hence the involvement of the active degradation agent can be arranged in the following sequence O_2*> *OH > *e* > h^+.

The Cu-TiO_2@g-C_3N_4 was tested for rhodamine B (RB), methyl red (MR), cationic dyes, and Congo red (CR), alizarin red (Aliz), and indigo carmine (IC) photodegradation. Within 60 minutes, the degradation percentages of the CR, Aliz and IC anionic dyes were in turn 74.8, 73.9 and 86.4 % which were higher than the cationic dyes RB (62.0 %) and MR (45.3 %) (Figures 6c and e). The kinetics of all the dyes degradation was found to side with the pseudo-first-order kinetics model (Figure 6d) and the tabulated data (Table 2) follow the degradation percentage trend. Thus it can be suggested that the Cu-TiO_2@g-C_3N_4 composite is suitable for both anionic at cationic dyes at neutral pH.

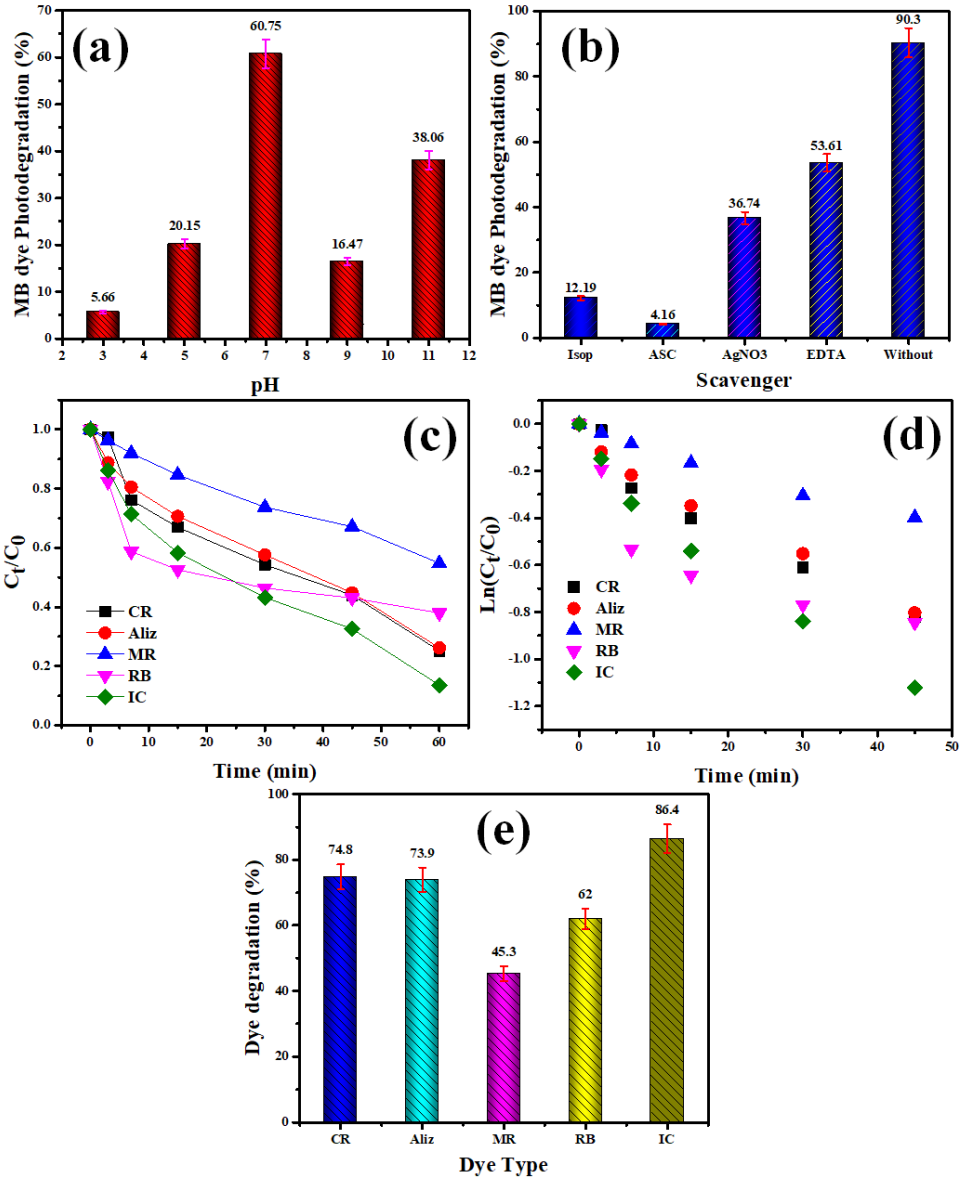

Figure 6. The pH (a) and radicals scavengers (b) on the MB photodegradation, and the degradation efficiency (c, e) and kinetics (d) graphs for multiple dye photodegradation.

To illusidate the MB photodegradation mechanism, the band gap energies of the g-C_3N_4 and Cu-TiO_2 were considered and the conduction (CB) and valence (VB) band edge positions of the semiconductor were calculated according to the Butler-Ginley equation [74]. The E_{CB} and E_{VB} for the g-C_3N_4 were respectively -1.275 and 1.715 eV respectively, whereas, the -0.355 and 2.975 eV were determined fo the Cu-TiO_2. According to the UV-visible absorption (Scheme 2), the Cu-TiO_2 seems incapable of visible light absorption and the subsequent excitation process, but the presence of some C and N on its surface can create inter-band states that enable visible light absorption as previously reported for ZnO/g-C_3N_4 core-shell nano-plates [75]. Thus, it is sensible to suggest a Z-scheme mechanism by creating a heterojunction between the Cu-TiO_2 and the g-C_3N_4. It is a well-established that heterogeneous photocatalysis processes generally proceed via four stages; starting with harvesting the light; followed by the photo-excitation of the charge-carrier; then the charge split-up and transporting the of charges to catalyst's surface ; and finally the redox reaction. The probable reactions involved in the MB photocatalytic degradation are as follows:

$$g - C_3N_4 + hv \rightarrow e_{CB}^- + h_{VB}^+ \quad \text{(i)}$$
$$Cu.TiO_2 + hv \rightarrow e_{CB}^- + h_{VB}^+ \quad \text{(ii)}$$
$$e_{CB}^- + O_2 \rightarrow * O_2^- \quad \text{(iii)}$$
$$O_2^{-^\circ} + 2H_2O + e_{CB}^- \rightarrow 3OH^- + * OH \quad \text{(iv)}$$
$$h_{VB}^+ + H_2O \rightarrow H^+ + * OH \quad \text{(v)}$$
$$MB + * OH \rightarrow CO_2 + H_2O \quad \text{(vi)}$$

Under visible light illumination, g-C_3N_4 and Cu-TiO_2 semiconductor would photo-excite and create electron-hole pairs. The photogenerated electron-hole pairs get separated and change to reverse directions as of in Z-scheme course and leads to suppressing the recombination rate. Briefly, when visible light is absorbed by g-C_3N_4 or the Cu-TiO_2 the electrons are excited to CB leaving the hole behind at VB. Thereafter the electron from CB of the Cu-TiO_2 can drift to the holes occupied VB of the g-C_3N_4 due to the attraction of the inherent electric field, and hence the likelihood of reconnecting the electron-hole pairs can be inhibited. The electrons in the CB of g-C_3N_4 can be trapped by O_2 to form $*O_2^-$ because the CB potential of g-C_3N_4 (−1.295 eV) is more negative than the standard redox potential of $O_2/*O_2^-$ (E° = -0.40 eV vs. NHE) [76] (equation iii). Bearing in mind the oxidation potentials of H_2O or OH^- (OH^- to *OH [E° = 2.38 V vs. NHE] (equation iv), and H_2O to *OH [E° = 1.99 eV vs. NHE] equation v), hence the VB of the Z-scheme heterojunction is 2.975 Ve vs. NHE, which is more anodic is adequate to breed the *OH. The scheme clearly supports the scavengers' experiment results the revealed the major roles of the O_2* and *OH radicals and the minor contribution of the e and h^+ entities which is associated with the generation of the radicals as indicated by equations *i-v*. Scheme 2 exemplifies the plausible Z-scheme for the MB degradation by the Cu-TiO_2@g-C_3N_4 composite.

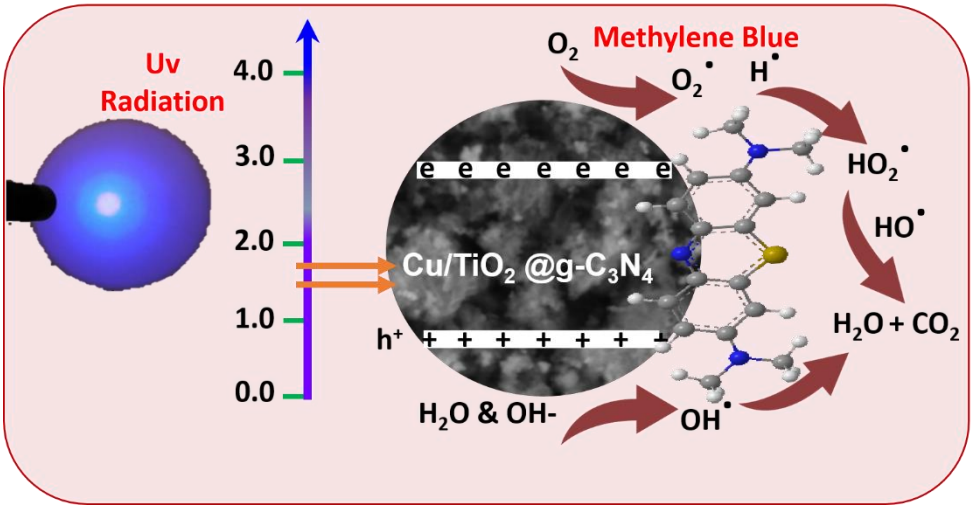

Scheme 2: The Cu-TiO_2@g-C_3N_4-MB photocatalysts mechanism.

4. Conclusion

In this research, a novel Cu-TiO_2@g-C_3N_4 composite was designed and fabricated using in situ synthetic protocol. The crystal structure, morphology, composition, and optical quality of the product were probed in detail using different identification techniques. The Cu-TiO_2 was evenly distributed in the nitride matrix, it was found to have narrow band gap energy and absorb in the visible light region. Its photocatalytic performance was tested by the photodegradation of the MB in aqueous solutions. The kinetics of the photodegradation followed the pseudo-first-order model with a rate constant that tripled compared to the Cu-TiO_2 due to nitride coupling. The O_2* and *OH radicals greatly influenced the dye decolorization process. The adopted simple strategy had realized the effective charge carriers separation for enhanced photocatalytic degradation aptitude.

Acknowledgment

"The authors gratefully acknowledge Qassim University, represented by the Deanship of Graduate Studies and Scientific Research, on the financial support for this research under the number (QU-J-PG-2-2025-53501) during the academic year 1446 AH / 2024 AD".

References

[1] R. Al-Tohamy, K. Singh, M.M. El-Sheekh, M. Nagy, S. Abdel-Satar, M.A. Ghoneim, A.S. Elkady, A.M. Khalil, A. Elella, E. Magdy, A. Antar, A. Hassanein, A. Mohamed, M. Yassin, and R. Zaki, A critical review on the treatment of dye-containing wastewater: Ecotoxicological and health concerns of textile dyes and possible remediation approaches for environmental safety, Ecotoxicology and Environmental Safety, 231 (2022) 113160.

[2] S. Parmar, R.K. Verma, A. Singh, P. Kumar, and J. Mishra, Microorganism: An ecofriendly tool for waste management and environmental safety, in Development in Wastewater Treatment Research and Processes, Elsevier, 2022, pp. 175-193.

[3] K. Singha, R. Sharma, N. Das, and M. Mukherjee, Harmful environmental effects for textile chemical dyeing practice, in Green Chemistry for Sustainable Textiles, Elsevier, 2021, pp. 153-164.

[4] A.C. Silva, L. Rodrigues, C. Alves, and J. Pereira, Modification of textiles for functional applications, in Fundamentals of Natural Fibres and Textiles, Elsevier, 2021, pp. 303-365.

[5] P. Faria, J. Orfao, and A. Pereira, Adsorption of aromatic compounds from the biodegradation of azo dyes on activated carbon, Applied Surface Science, 254 (2008) 3497-3503.

[6] S. Dutta, and J. Bhattacharjee, A comparative study between physicochemical and biological methods for effective removal of textile dye from wastewater, in Development in Wastewater Treatment Research and Processes, Elsevier, 2022, pp. 1-21.

[7] A. Azanaw, S. Getahun, M. Assefa, and T. Teshome, Textile effluent treatment methods and eco-friendly resolution of textile wastewater, Case Studies in Chemical and Environmental Engineering, 6 (2022) 100230.

[8] B. Lellis, C. Fávaro-Polonio, J. Pamphile, and M. Polonio, Effects of textile dyes on health and the environment and bioremediation potential of living organisms, Biotechnology Research and Innovation, 3 (2019) 275-290.

[9] M. S. Saddik, M. M. Elsayed, A. A. Abdel-Rheem, M. A. El-Mokhtar, E. S. Mosa, M. F. Al-Hakkani, S. A. Al-Shelkamy, A. Khames, M. A. Daha, and J. A. Abdel-Aleem, A novel C@Fe@Cu nanocomposite loaded with doxorubicin tailored for the treatment of hepatocellular carcinoma, Pharmaceutics, 14 (2022) 1845.

[10] A. E. Albadri, M. A. Ben Aissa, A. Modwi, and S. M. Saleh, Synthesis of mesoporous Ru-ZnO@g-C_3N_4 nanoparticles and their photocatalytic activity for methylene blue degradation, in Water, MDPI, 15(3) (2023) 481.

[11] A. A. Hanna, W. A. A. Mohamed, and I. A. Ibrahim, Studies on photodegradation of Methylene Blue (MB) by nano-sized titanium oxide, Egyptian Journal of Chemistry, 57(4) (2014) 315-325.

[12] A. M. Younis, F. M. Alminderej, A. H. Alluhayb, S. M. Saleh, M. A. Ben Aissa, and A. Modwi, Synergistic adsorption of methylene blue from aqueous medium using MgO-Y_2O_3@gC_3N_4 (MYCN) nanocomposite: Performance evaluation and kinetic study, in Nano-Structures & Nano-Objects, 39 (2024)101267.

[13] S. M. Saleh, Metal oxide nanomaterials as photo-catalyst for dye degradation, Research & Development in Materials Science, 9 (2019) 1-8.degradatuino

[14] H. H. A. Ghafar, T. Salem, E. K. Radwan, A. A. El-Sayed, M. A. Embaby, and M. Salama, Modification of waste wool fiber as low-cost adsorbent for the removal of methylene blue from aqueous solution, Egyptian Journal of Chemistry, 60(3) (2017) 395-406.

[15] S. M. Saleh, ZnO nanospheres based simple hydrothermal route for photocatalytic degradation of azo dye, in Spectrochimica Acta Part A: Molecular and Biomolecular Spectroscopy, 211 (2019) 141-147.

[16] R. Foroutan, R. Mohammadi, and B. Ramavandi, Elimination performance of methylene blue, methyl violet, and Nile blue from aqueous media using AC/$CoFe_2O_4$ as a recyclable magnetic composite, Environmental Science and Pollution Research, 26 (2019) 19523-19539.

[17] M. A. Ben Aissa, A. Modwi, A. E. Albadri, and S. M. Saleh, Dependency of crystal violet dye removal behaviors onto mesoporous V_2O_5-g-C_3N_4 constructed by simplistic ultrasonic method, Inorganics, 11 (2023) 146.

[18] F.E. Titchou, A. Elfakir, M. Boujjat, and M. Laamarti, Batch elimination of cationic dye from aqueous solution by electrocoagulation process, Mediterranean Journal of Chemistry, 10 (2020) 1-12.

[19] F. M. Alminderej, A. E. Albadri, Y. El-Ghoul, W. A. El-Sayed, A. M. Younis, and S. M. Saleh, Sustainable and green synthesis of carbon nanofibers from date palm residues and their adsorption efficiency for eosin dye, Sustainability, 15 (2023) 10451.

[20] Z. Mo, L. Han, H. Wang, Y. Zhao, and T. Zhu, Synthesis of g-C_3N_4 at different temperatures for superior visible/UV photocatalytic performance and photoelectrochemical sensing of MB solution, RSC Advances, 5 (2015) 101552-101562.

[21] S. M. Saleh, A. E. Albadri, M. A. Ben Aissa, and A. Modwi, Fabrication of mesoporous V_2O_5@g-C_3N_4 nanocomposite as photocatalyst for dye degradation, Crystals, 12 (2022) 1766.

[22] S. Alkaykh, A. Mbarek, and E.E. Ali-Shattle, Photocatalytic degradation of methylene blue dye in aqueous solution by $MnTiO_3$ nanoparticles under sunlight irradiation, Heliyon, 6 (2020).

[23] D. P. Kotla, V. R. Anna, S. Praveenkumar, S. M. Saleh, and S. Shanmugan, Optimizing solar still performance: A study of TiO_2 nanofluid derived from Saccharum officinarum L., Separation and Purification Technology, 359 (2025) 130584.

[24] B. R. Alsehli, F. M. Alminderej, M. H. Hassan, M. F. Al-Hakkani, S. M. Saleh, and D. S. Mohamed, Biosynthesis, characterizations, and comparison of TiO_2/CeO_2/their nanocomposites as bio-adsorbents of linezolid and their microbiological activities, Journal of Molecular Structure, 1328

[25] C.B. Anucha, P. Ekpo, J. Obot, and R. Enoma, Titanium dioxide (TiO_2)-based photocatalyst materials activity enhancement for contaminants of emerging concern (CECs) degradation: In the light of modification strategies, Chemical Engineering Journal Advances, 10 (2022) 100262.

[26] M. H. Omar, A. E. M. Elfarash, H. M. El-Aref, and M. F. Al-Hakkani, Role of biosynthesized titanium dioxide nanoparticles in antibacterial activity and cefoperazone removal from pharmaceutical wastewater, Process Biochemistry, 142 (2024) 162-174.

[27] G. Orizu, J. Uchenna, J. Newman, and D. Okoro, A review on the inference of doping TiO_2 with metals/non-metals to

improve its photocatalytic activities, in IOP Conference Series: Earth and Environmental Science, 2023, IOP Publishing.
[28] A. Aljaafari, Effect of metal and non-metal doping on the photocatalytic performance of titanium dioxide (TiO_2): A review, Current Nanoscience, 18 (2022) 499-519.
[29] M. Hasanuzzaman, J. Sadiq, A. Haque, and S. Moniruzzaman, Co-doped (N and Fe) TiO_2 photosensitising nanoparticles and their applications: A review, Advances in Materials and Processing Technologies (2023) 1–24.
[30] D. Kolli, S. Biswas, A. V. Rao, S. M. Saleh, and S. Shanmugan, Modulating ZnO nanoparticle photoluminescence through Ce^{3+}-induced defect engineering: A study of microstructural and spectroscopic properties, Ceramics International, 51 (2025) 8472-8479.
[31] S. Singla, S. Sharma, and S. Basu, MoS_2/WO_3 heterojunction with the intensified photocatalytic performance for decomposition of organic pollutants under the broad array of solar light, Journal of Cleaner Production, 324 (2021) 129290.
[32] R. A. Alkhalifa, A. E. Albadri, R. Ali, A. H. Alluhayb, A. M. Younis, and S. M. Saleh, Sustainable synthesis of zirconium dioxide (ZrO_2) nanoparticles utilizing Asphodelus fistulosus extract for Congo red degradation, Catalysts, 15 (2025) 123.
[33] R. Del Angel, J.C. Durán-Álvarez, and R. Zanella, TiO_2-low band gap semiconductor heterostructures for water treatment using sunlight-driven photocatalysis, Titanium Dioxide: Material for a Sustainable Environment, 305 (2018).
[34] F. K. Alharbi, M. A. Ben Aissa, A. Modwi, A. A. Alharbi, F. Alfadhl, and S. M. Saleh, Impact of Ag-NiO nanoparticles loaded on g-C_3N_4 nanosheets for cleaning contaminated water, Inorganic Chemistry Communications, 166 (2024) 112608.
[35] F. K. Alharbi, A. E. Albadri, A. Modwi, and S. M. Saleh, Effectiveness of Ag@NiO@g-C_3N_4 photocatalysts: Green fabrication and superior photocatalysis capability, Optical Materials, 152 (2024) 115410.
[36] M. Ismail, A. E. Albadri, M. A. Ben Aissa, A. Modwi, and S. M. Saleh, High poisonous Cd ions removal by Ru-ZnO-g-C_3N_4 nanocomposite: description and adsorption mechanism, Inorganics, 11 (2023) 176.
[37] X. Wu, J. Zhang, C. He, and L. Huang, Soluble g-C_3N_4 nanosheets: Facile synthesis and application in photocatalytic hydrogen evolution, Applied Catalysis B: Environmental, 247 (2019) 70-77.
[38] H. Jiang, X. Wang, J. Li, and Z. Zhang, Recent advances in heteroatom doped graphitic carbon nitride (g-C_3N_4) and g-C_3N_4/metal oxide composite photocatalysts, Current Organic Chemistry, 24 (2020) 673-693.
[39] S. Kumar, P.-H. Weng, and Y.-P. Fu, NiO/g-C_3N_4/PANI/Ni-metal-organic framework composite for high-energy supercapacitor electrodes, Materials Today Chemistry, 28 (2023) 101385.
[40] E. Chamanehpour, M.H. Sayadi, and M. Hajiani, Metal-organic framework coordinated with g-C3N4 and metal ions for boosting photocatalytic H_2 production under sunlight, Journal of Photochemistry and Photobiology A: Chemistry, 434 (2023) 114221.
[41] M. Inagaki, H. Tsumura, Y. Miyagawa, and Y. Hishiyama, Graphitic carbon nitrides (g-C_3N_4) with comparative discussion to carbon materials, Carbon, 141 (2019) 580-607.
[42] D. Zhou and C. Qiu, Study on the effect of Co doping concentration on optical properties of g-C_3N_4, Chemical Physics Letters, 728 (2019) 70-73.
[43] A.V. Vorontsov and S.V. Tsybulya, Influence of nanoparticles size on XRD patterns for small monodisperse nanoparticles of Cu^0 and TiO_2 anatase, Industrial & Engineering Chemistry Research, 57 (2018) 2526-2536.
[44] C.-J. Lin and W.-T. Yang, Ordered mesostructured Cu-doped TiO_2 spheres as active visible-light-driven photocatalysts for degradation of paracetamol, Chemical Engineering Journal, 237 (2014) 131-137.
[45] X. Zheng, L. Yu, R. Zhang, and T. Wang, Electrospinning Cu–TiO_2 nanofibers used for photocatalytic disinfection of bacteriophage f2: Preparation, optimization and characterization, RSC Advances, 7 (2017) 52172-52179.
[46] D. Tobaldi, M. Pina, G. Leroy, and P. Rocha, Cu–TiO_2 hybrid nanoparticles exhibiting tunable photochromic behavior, The Journal of Physical Chemistry C, 119 (2015) 23658-23668.
[47] H. Liyanaarachchi, N. Gunasekara, R. Malaviarachchi, and J. Premachandra, Efficient photocatalysis of Cu-doped TiO_2/g-C_3N_4 for the photodegradation of methylene blue, Arabian Journal of Chemistry, 16 (2023) 104749.
[48] G.V. Jensen, B. Keller, S. Vagners, and E. Campbell, Anisotropic crystal growth kinetics of anatase TiO_2 nanoparticles synthesized in a nonaqueous medium, Chemistry of Materials, 22 (2010) 6044-6055.
[49] D.O. Adekoya, M.B. Tahir, and N.A.S. Amin, g-C_3N_4/(Cu/TiO_2) nanocomposite for enhanced photoreduction of CO_2 to CH_3OH and HCOOH under UV/visible light, Journal of CO_2 Utilization, 18 (2017) 261-274.
[50] M. Alavi, N. Karimi, and T. Valadbeigi, Antibacterial, antibiofilm, antiquorum sensing, antimotility, and antioxidant activities of green fabricated Ag, Cu, TiO_2, ZnO, and Fe_3O_4 NPs via Protoparmeliopsis muralis lichen aqueous extract against multi-drug-resistant bacteria, ACS Biomaterials Science & Engineering, 5 (2019) 4228-4243.
[51] Y. Nakabayashi and Y. Nosaka, The pH dependence of OH radical formation in photo-electrochemical water oxidation with rutile TiO_2 single crystals, Physical Chemistry Chemical Physics, 17 (2015) 30570-30576.
[52] A. Alsalme, H. Almulaiky, A. Shater, and A. Alsulami, Fabrication of S-scheme TiO_2/g-C_3N_4 nanocomposites for generation of hydrogen gas and removal of fluorescein dye, Diamond and Related Materials, 122 (2022) 108819.
[53] R. Acharya and K. Parida, A review on TiO_2/g-C_3N_4 visible-light-responsive photocatalysts for sustainable energy generation and environmental remediation, Journal of Environmental Chemical Engineering, 8 (2020) 103896.
[54] B. Yu, C. Zhao, F. Yuan, X. Wang, and T. Zhao, Facile synthesis of AgNPs modified TiO_2@g-C_3N_4 heterojunction composites with enhanced photocatalytic activity under simulated sunlight, Materials Research Bulletin, 121 (2020) 110641.
[55] G. Wang, H. He, J. Zhang, L. Zhang, and X. Wei, Highly efficient photocatalytic oxidation of antibiotic ciprofloxacin using TiO_2@g-C_3N_4@biochar composite, Environmental Science and Pollution Research, 29 (2022) 48522-48538.
[56] K. Baishya, A. Sharma, B. Gogoi, and R. Das, Graphene-mediated band gap engineering of WO_3 nanoparticle and a relook at Tauc equation for band gap evaluation, Applied Physics A, 124 (2018) 1-6.
[57] A.Z. Johannes, R.K. Pingak, and M. Bukit, Tauc Plot Software: Calculating energy gap values of organic materials based

on ultraviolet-visible absorbance spectrum, in IOP Conference Series: Materials Science and Engineering, 2020, IOP Publishing.
[58] S. Chen, J. Li, Y. Guo, Q. Wu, and Z. Tang, Fabrication and characterization of novel Z-scheme photocatalyst WO_3/g-C_3N_4 with high efficient visible light photocatalytic activity, Materials Chemistry and Physics, 149 (2015) 512-521.
[59] D. F. Katowah, S. M. Saleh, S. A. Alqarni, R. Ali, G. I. Mohammed, and M. A. Hussein, Network structure-based decorated CPA@CuO hybrid nanocomposite for methyl orange environmental remediation, Scientific Reports, 11 (2021) 5056.
[60] D. F. Katowah, S. M. Saleh, G. I. Mohammed, N. S. Alkayal, R. Ali, and M. A. Hussein, Ultra-efficient hybrid material-based cross-linked PANI@Cs-GO-OXS/CuO for the photocatalytic degradation of Rhodamine-B, Journal of Physics and Chemistry of Solids, 157 (2021) 110208.
[61] C. Boruban and E.N. Esenturk, Activated carbon-supported CuO nanoparticles: A hybrid material for carbon dioxide adsorption, Journal of Nanoparticle Research, 20 (2018) 1-9.
[62] Y. He, F. Li, J. Zhu, X. Wu, and Q. Wang, Encapsulation of highly dispersed Au NPs by strong metal–support interactions in porous titania nanoplates for efficient electrosynthesis of H_2O_2, Advanced Functional Materials (2024) 2314654.
[63] G.B. Yitagesu, D.T. Leku, and G.A. Workneh, Green synthesis of TiO_2 using Impatiens rothii Hook. f. leaf extract for efficient removal of methylene blue dye, ACS Omega, 8 (2023) 43999-44012.
[64] D. Hariharan, R. Venkatraman, and A. Renganathan, Visible light active photocatalyst: Hydrothermal green synthesized TiO_2 NPs for degradation of picric acid, Materials Letters, 222 (2018) 45-49.
[65] Z. Chen, L. Xiao, J. Ma, R. Duan, and S. Lin, Merging single-atom-dispersed silver and carbon nitride to a joint electronic system via copolymerization with silver tricyanomethanide, ACS Nano, 10 (2016) 3166-3175.
[66] H. Dou, S. Wang, Y. Wei, R. Zhang, and T. Zhang, Core–shell g-C_3N_4/Pt/TiO_2 nanowires for simultaneous photocatalytic H2 evolution and RhB degradation under visible light irradiation, Catalysis Science & Technology, 9 (2019) 4898-4908.
[67] B. Lv, J. Zhang, Q. Luo, Y. Yang, and M. Zhu, Efficient photocatalytic hydrogen production using an NH_4TiOF_3/TiO_2/g-C_3N_4 composite with a 3D camellia-like Z-scheme heterojunction structure, Ceramics International, 46 (2020) 26689-26697.
[68] L. Shen, W. Guo, X. Deng, H. Fang, and Z. Xie, Black TiO_2 nanobelts/g-C_3N_4 nanosheets laminated heterojunctions with efficient visible-light-driven photocatalytic performance, Scientific Reports, 7 (2017) 41978.
[69] H.Y. Hafeez, M.A. Basit, Z. Khan, A. Javaid, and M. Umar, Insights into hybrid TiO_2-g-C_3N_4 heterostructure composite decorated with rGO sheet: A highly efficient photocatalyst for boosted solar fuel (hydrogen) generation, Chemical Physics Impact, 6 (2023) 100157.
[70] M. Saeed, H. Naveed, Z. Tariq, Y. Javed, and M. Waqas, Photocatalysis: An effective tool for photodegradation of dyes-A review, Environmental Science and Pollution Research, 29 (2022) 293-311.
[71] V. Gadore, S.R. Mishra, and M. Ahmaruzzaman, Metal sulphides and their heterojunctions for photocatalytic degradation of organic dyes-A comprehensive review, Environmental Science and Pollution Research, 30 (2023) 90410-90457.
[72] J. Yao and C. Wang, Decolorization of methylene blue with TiO_2 sol via UV irradiation photocatalytic degradation, International Journal of Photoenergy, 2010 (2010) 643182.
[73] C. Yavuz and S. Erten-Ela, Solar light-responsive α-Fe_2O_3/CdS/g-C_3N_4 ternary photocatalyst for photocatalytic hydrogen production and photodegradation of methylene blue, Journal of Alloys and Compounds, 908 (2022) 164584.
[74] H.G. Gebreegziabher, Y.B. Yicheneku, and G.K. Weldegebrieal, Synthesis of NiO nanoparticles using chemical precipitation method for the photocatalytic degradation of methylene blue dye, Journal of Cleaner Production, 2024 (2024).
[75] S. Kumar, S. Verma, A. Mishra, and P.-H. Weng, Cost-effective and eco-friendly synthesis of novel and stable N-doped ZnO/g-C_3N_4 core–shell nanoplates with excellent visible-light responsive photocatalysis, Nanoscale, 6 (2014) 4830-4842.
[76] B. Li, Y. Pan, R. Fang, and Q. Zhou, Novel synthesis of Z-scheme α-Bi_2O_3/g-C_3N_4 composite photocatalyst and its enhanced visible light photocatalytic performance: Influence of calcination temperature, Chinese Chemical Letters, 31 (2020) 2705-2711.